Applied Physics B (2018) 124:55
https://doi.org/10.1007/s00340-018-6921-1

Applied Physics B
Lasers and Optics

Non-destructive testing of ceramic materials using mid-infrared ultrashort-pulse laser

S. C. Sun[1] · Hong Qi[1] · X. Y. An[1] · Y. T. Ren[1] · Y. B. Qiao[1] · Liming M. Ruan[1]

Received: 14 December 2017 / Accepted: 1 March 2018 / Published online: 14 March 2018

Abstract

The non-destructive testing (NDT) of ceramic materials using mid-infrared ultrashort-pulse laser is investigated in this study. The discrete ordinate method is applied to solve the transient radiative transfer equation in 2D semitransparent medium and the emerging radiative intensity on boundary serves as input for the inverse analysis. The sequential quadratic programming algorithm is employed as the inverse technique to optimize objective function, in which the gradient of objective function with respect to reconstruction parameters is calculated using the adjoint model. Two reticulated porous ceramics including partially stabilized zirconia and oxide-bonded silicon carbide are tested. The retrieval results show that the main characteristics of defects such as optical properties, geometric shapes and positions can be accurately reconstructed by the present model. The proposed technique is effective and robust in NDT of ceramics even with measurement errors.

List of symbols

A	Set of all restriction
b	Weight coefficient
c	Speed of light (m/s)
c_i	Restriction
d	Search direction
f	Parameter of DRIFD phase function
E	Set of equality restriction
F	Objective function
g	Parameter of H–G phase function
H	Heaviside step function or approximation of the Hessian
I	Radiative intensity, W/(m^2 sr)
k	Iteration number
L	Size of medium
m	Number of restriction
m_e	Number of equality restriction
min	Minimize
n	Refractive index
n	Normal vector
N	Number of grid or set of all neighboring pixel pairs
NN	Total number of the parameter to be reconstructed
NΩ	Number of discretized direction
p	Sharpness parameter
r	Penalty factor
r	Position
R	Emerging radiative intensity
s_0	Transmission distance of the collimated intensity
s.t.	Subject to
S	Source term (W/m^3)
t	Time (s)
t_p	Pulse width of laser (s)
u_i	Lagrangian multiplier in SQP
w	Directional weight
x	Parameter to be reconstructed or coordinate in *x* direction (m)
y	Coordinate in *y* direction (m)

Greeks symbols

α	Search step size
β	A positive value
β_e	Extinction coefficient (m^{-1})
δ	Dirac's delta function
ε	Convergence accuracy
Δt	Time step (s)

This article is part of the topical collection "Mid-infrared and THz Laser Sources and Applications" guest edited by Wei Ren, Paolo De Natale and Gerard Wysocki.

✉ Hong Qi
qihong@hit.edu.cn

✉ Liming M. Ruan
ruanlm@hit.edu.cn

[1] School of Energy Science and Engineering, Harbin Institute of Technology, 92, West Dazhi Street, Harbin 150001, People's Republic of China

Δx	Grid size in x direction
Δy	Grid size in y direction
η	Directional cosines of y direction
ϑ	Scale parameter
κ_a	Absorption coefficient (m^{-1})
κ_s	Scattering coefficient (m^{-1})
λ_i	Lagrangian multiplier in adjoint model
$\boldsymbol{\Omega}$	Scattering direction
$\boldsymbol{\Omega}'$	Incident direction
υ	A small positive value
ξ	Directional cosines in x direction
$\mathfrak{R}$	Regularization term

Subscripts

bck	Back scattering
est	Estimated value
exa	Exact value
c	Collimated value or central point
d	Diffused value
D	Computational domain
DIFF	Diffraction-dominated
DIF RER	Diffusely reflective
hg	Henyey–Greenstein
is	Isotropically scattering
l	lth discretized direction
∂D	Boundary of computational domain
m	mth discretized direction
max	The maximum value
p	Penalty function
t	Time
u	Neighboring position
v	Neighboring position
x	x direction
y	y direction
xu	Upstream position in x direction
yu	Upstream position in y direction

1 Introduction

Ceramics are widely applied in aerospace industries such as ram jet engines, space shuttle, aerocraft, turbine engines, to name a few [1–7]. Generally, the ceramic materials in these areas usually work in high temperature and aggressive environments. Thus, accurate and effective non-destructive testing (NDT) technique is fundamentally important to guarantee the quality of ceramics [8–11]. Over the last few decades, there has been a significant amount of interest in the development of NDT technique and a wide range of new sensing methodologies are successfully applied to the NDT of ceramics, such as X-ray computed tomography (X-ray CT) [12], ultrasonic testing (UT) [13], acoustic emission [14], microwave interferometry [15], holographic interferometry [16], etc. However, all of these methods have limitations on the type of defects to be detected or the type of materials that can be inspected. For example, the depth of defects cannot be clearly identified by the X-ray CT. Complex geometry may reduce the evaluation accuracy of UT and it is necessary to make the wavelength comparable to defect size for UT technique [17, 18].

Infrared thermography is an effective non-destructive evaluation technology which can achieve high detection accuracy and sensitivity. Infrared NDT technique has many advantages such as non-contact measurement, ease of use and resistance to electromagnetic interference and thereby it gets more and more attentions. Numerous thermography NDT techniques including infrared thermal imaging [19], pulsed transient thermography [20, 21], thermal-wave radar imaging (TWRI) [5] and lock-in thermography (LIT) [22–24] are successfully employed to detect the defects in various materials. Ludwig and Peruzzi [25] applied video pulse thermography technique to detect the circular subsuperficial defects in structural components. The time evolution of the full-width half-maximum of thermal contrast was investigated by theoretical and experimental methods. However, a significant mismatch was obtained between the theoretical and experimental results, which may be due to the heat losses caused by radiation and convection neglected in the theoretical research. Maldague et al. [26] proposed a double-pulse infrared thermography technique to improve the detectable depth of defects in specimen. Two separated heating pulses not only reduced the importance of high frequency of incident laser and enhanced signal-to-noise ratio, but also facilitated reproducing experiments. Meanwhile, the optimum interval between two pulses was given based on experimental studies. Gong et al. [5] studied the NDT for carbon fiber-reinforced polymer through the TWRI technique. The multi-transform techniques such as Fourier transform, Hilbert transform and cross-correlation were employed to extract the characteristics of thermal-wave signals. The subsurface defects were investigated both theoretically and experimentally. Busse et al. [24] proposed the LIT technique, in which the thermography and thermal-wave techniques were combined to provide short-time low-frequency phase angle images. Compared with infrared thermography technique, LIT can provide additional phase information which will be not affected by the environmental noise and emissivity of specimen. Also, an increased depth range at a short time can be obtained, which demonstrated the superiority of LIT technique. However, all of the above thermography NDT techniques are based on the thermal response on surfaces, the power and frequency of incident laser should be reasonably controlled. Moreover, most of the infrared

thermography methods are analyzed by using heat conduction model, which may produce large mismatches between simulation and experimental results, especially for high-temperature semitransparent materials.

Optical imaging is a novel detection methodology occurs with the development of ultrashort-pulse laser. The propagation of photon is considered as a transient process, which can provide much more information for the inverse analysis than steady radiative transfer model [27–29]. Nowadays, the optical tomography technique has been widely applied in biomedical areas due to the near-infrared laser has little damage to biological issue [30–34]. For instance, Hebden et al. [30] investigated the blood oxygenation changes in the newborn infant brain using optical tomography. The pulse lasers at wavelengths 780 and 815 nm were employed as the illumination source. The retrieved results showed that the absorption coefficients at two wavelengths were significantly different. The imaging results of the difference between oxyhemoglobin and deoxyhemoglobin were in good agreement with the physiological data. Li et al. [32] studied clinic detection in breast tissue based on the near-infrared optical imaging technique. The dual-wavelength near-infrared light was applied to detect the breast and the highly sensitive charge coupled device was employed as the detector. The clinical experiments demonstrated that the malignant tumor usually higher hemoglobin concentration and lower oxygen saturation, while the benign lesion was the opposite. Wan and Guo [33] simulated the changes of cerebral blood oxygen saturation through the Monte Carlo method. The optical reflectance was employed as the measurement signal and the reflectance ratios between two wavelengths at 633 and 800 nm were measured under different blood vessel levels. A quantifiable correlation between the reflectance ratio and the cerebral blood oxygen saturation was obtained.

To the best knowledge of the authors, the application of ultrashort-pulse laser in NDT has not yet been reported. For the reticulated porous ceramics introduced in Ref. [1], the absorption coefficient is close to 0 while the scattering coefficient is about 10^3 m^{-1} in the near-infrared spectral range, which may lead to the radiative transfer process being dominated by the scattering coefficient and the absorption coefficient cannot be accurately reconstructed. On the contrary, the difference between the absorption and scattering coefficients is relatively small in the mid-infrared spectral range, which provides a good research area for simultaneous reconstruction. The current study aims to non-destructively detect the defects in ceramic materials using mid-infrared ultrashort-pulse laser. The transient (time-domain) radiative transfer is considered to describe the transmission of laser in ceramics. Two reticulated porous ceramics, partially stabilized zirconia (PS ZrO_2) and oxide-bonded silicon carbide (OB SiC), are tested by the present model numerically. The reminder of this work is organized as follows. In Sect. 2, the 2D transient radiative transfer equation (TRTE) in semitransparent medium is introduced and the principle of discrete ordinate method (DOM) for solving the direct problem is discussed. The gradient of objective function with respect to the absorption and scattering coefficients is solved by the adjoint equation, which is presented in Sect. 3. The theoretical overview of sequential quadratic programming (SQP) is described in Sect. 4. In Sect. 5, the NDT results of ceramics are presented. The effects of spatial position, total number and geometric shapes of defects on the detection results are also discussed. The main conclusions are provided in Sect. 6.

2 Direct problem

As shown in Fig. 1, the 2D semitransparent medium exposed to a collimated laser irradiation is considered here. The 2D TRTE can be expressed as [35, 36]:

$$\frac{n}{c}\frac{\partial I(\mathbf{r},\mathbf{\Omega},t)}{\partial t}+\Omega\cdot\nabla I(\mathbf{r},\mathbf{\Omega},t)=-\beta_{\mathrm{e}}(\mathbf{r})I(\mathbf{r},\mathbf{\Omega},t)+\frac{\kappa_s(r)}{4\pi}\int_{4\pi}I(\mathbf{r},\mathbf{\Omega}',t)\Phi(\mathbf{\Omega}',\mathbf{\Omega})\mathrm{d}\Omega', \tag{1}$$

where n is the refractive index. c is the velocity of light. β_{e} and κ_{s} represent the extinction coefficient and scattering coefficient, respectively. If the absorption coefficient is denoted by κ_{a}, $\beta_{\mathrm{e}}=\kappa_{\mathrm{a}}+\kappa_{\mathrm{s}}$, $\mathbf{\Omega}'$ and $\mathbf{\Omega}$ indicate the incident and the scattering directions, respectively. Φ represents the scattering phase function. Two dual-parameter phase functions are considered to simulate the scattering characteristic of ceramics. The first one is based on the physical structure of reticulated porous ceramics which is written as [37]:

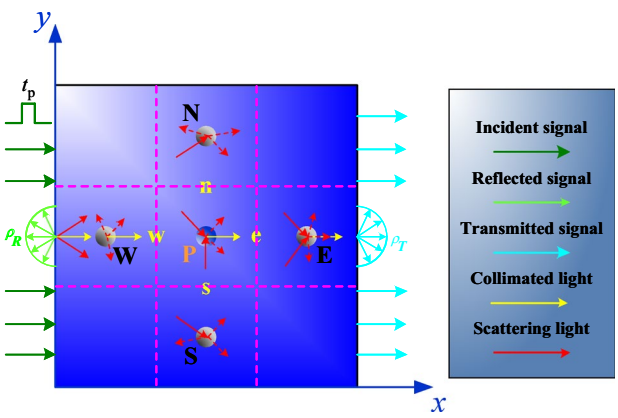

Fig. 1 Schematic of 2D participating medium

$$\Phi(\mathbf{\Omega}', \mathbf{\Omega}) = f_{\mathrm{iS}} + (1 - f_{\mathrm{iS}} - f_{\mathrm{bck}})\Phi_{\mathrm{DIFF}}(\mathbf{\Omega}', \mathbf{\Omega}) + f_{\mathrm{bck}}\Phi_{\mathrm{DIF\,RER}}(\mathbf{\Omega}', \mathbf{\Omega}), \tag{2}$$

where f_{is} and f_{bck} are fractions of isotropically and back scattering factors, respectively, and they satisfy $f_{\mathrm{iS}} - f_{\mathrm{bck}} \leqslant 1$. Φ_{DIFF} and $\Phi_{\mathrm{DIF\,RER}}$ represent the diffraction-dominated and diffusely reflective phase functions, respectively. It is called diffuse-reflectance, isotropic forward-diffraction (DRIFD) scattering phase function. The other phase function is the modified Henyey–Greenstein (H–G) phase function which can be expressed as:

$$\Phi(\mathbf{\Omega}', \mathbf{\Omega}) = f_{\mathrm{iS}} + (1 - f_{\mathrm{iS}})\frac{1 - g_{\mathrm{hg}}^2}{[1 + g_{\mathrm{hg}}^2 - 2g_{\mathrm{hg}} \cdot \cos(\mathbf{\Omega}', \mathbf{\Omega})]^{3/2}}, \tag{3}$$

where g_{hg} is the scattering asymmetry factor, $-1 \leqslant g_{\mathrm{hg}} \leqslant 1$.

The radiative intensity in the semitransparent media is composed of collimated intensity and diffused intensity, which can be written as:

$$I(\mathbf{r}, \mathbf{\Omega}, t) = I_{\mathrm{c}}(\mathbf{r}, \mathbf{\Omega}, t) + I_{\mathrm{d}}(\mathbf{r}, \mathbf{\Omega}, t), \tag{4}$$

where I_{d} and I_{c} represent the diffused radiative intensity that scattered from the radiative source and the remaining collimated radiative intensity, respectively. Hence, the TRTE can be expressed as:

$$\begin{aligned}\frac{n}{c}\left[\frac{\partial I_{\mathrm{c}}(\mathbf{r}, \mathbf{\Omega}, t)}{\partial t} + \frac{\partial I_{\mathrm{d}}(\mathbf{r}, \mathbf{\Omega}, t)}{\partial t}\right] + \mathbf{\Omega} \cdot \nabla(I_{\mathrm{c}}(\mathbf{r}, \mathbf{\Omega}, t) + I_{\mathrm{d}}(\mathbf{r}, \mathbf{\Omega}, t)) \\ = -\beta_{\mathrm{e}}(\mathbf{r})\left[I_{\mathrm{c}}(\mathbf{r}, \mathbf{\Omega}, t) + I_{\mathrm{d}}(\mathbf{r}, \mathbf{\Omega}, t)\right] \\ + \frac{\kappa_{\mathrm{s}}(\mathbf{r})}{4\pi}\int_{4\pi}[I_{\mathrm{c}}(\mathbf{r}, \mathbf{\Omega}', t) + I_{\mathrm{d}}(\mathbf{r}, \mathbf{\Omega}', t)]\Phi(\mathbf{\Omega}, \mathbf{\Omega}')\mathrm{d}\Omega.\end{aligned} \tag{5}$$

The variation of the collimated intensity at location $\mathbf{r}$ and time t in direction Ω satisfies the following Bouguer–Beer law [35]:

$$\frac{n}{c}\left[\frac{\partial I_{\mathrm{c}}(\mathbf{r}, \mathbf{\Omega}, t)}{\partial t} + \frac{\partial I_{\mathrm{d}}(\mathbf{r}, \mathbf{\Omega}, t)}{\partial r}\right] = -\beta_{\mathrm{e}}(\mathbf{r})I_{\mathrm{c}}(\mathbf{r}, \mathbf{\Omega}, t). \tag{6}$$

For a square pulse laser irradiation, the collimated intensity in the direction Ω_0 can be written as:

$$\begin{aligned}I_{\mathrm{c}}(\mathbf{r}, \mathbf{\Omega}, t) = I_{\mathrm{in}}\exp\left[-\int_0^{s_0}\beta_{\mathrm{e}}(\mathbf{r})\mathrm{d}r\right]\left[H(ct - s_0)\right. \\ \left. -H(ct - ct_p - s_0)\right]\delta(\mathbf{\Omega} - \mathbf{\Omega}_0),\end{aligned} \tag{7}$$

where Ω_0 represents the incident direction of laser. s_0 is the transmission distance of the collimated intensity. H is the Heaviside step function, and δ denotes the Dirac's delta function. t_{p} indicates the pulse width of laser. Thus, Eq. (5) can be presented by:

$$\begin{aligned}\frac{n}{c}\frac{\partial I_{\mathrm{d}}(\mathbf{r}, \mathbf{\Omega}, t)}{\partial t} + \partial I_{\mathrm{d}}(\mathbf{r}, \mathbf{\Omega}, t) = -\beta_{\mathrm{e}}(\mathbf{r})I_{\mathrm{d}}(\mathbf{r}, \mathbf{\Omega}, t) \\ + \frac{\kappa_{\mathrm{s}}(\mathbf{r})}{4\pi}\int_{4\pi} I_{\mathrm{d}}(\mathbf{r}, \mathbf{\Omega}', t)\Phi(\mathbf{\Omega}, \mathbf{\Omega}')\mathrm{d}\Omega' + S_{\mathrm{c}}(\mathbf{r}, \mathbf{\Omega}, t),\end{aligned} \tag{8}$$

where S_{c} represents the source term by the collimated intensity, which can be expressed as:

$$S_{\mathrm{c}}(\mathbf{r}, \mathbf{\Omega}, t) = \frac{\kappa_{\mathrm{s}}(\mathbf{r})}{4\pi}\int_{4\pi} I_{\mathrm{d}}(\mathbf{r}, \mathbf{\Omega}', t)\Phi(\mathbf{\Omega}, \mathbf{\Omega}')\mathrm{d}\Omega'. \tag{9}$$

The DOM is one of the most effective methods for solving radiative transfer problems in terms of computational accuracy and efficiency. The DOM had been proved to be more efficient to describe the short-pulse laser transfer than other methods such as the discrete transfer method and finite volume method [38]. Thus, the DOM is employed to solve the direct model and the discretized TRTE can be written as:

$$\begin{aligned}\frac{n}{c}\frac{\partial I^m_{\mathrm{d},t,x,y}}{\partial t} + \xi^m\frac{\partial I^m_{\mathrm{d},t,x,y}}{\partial x} + \eta^m\frac{\partial I^m_{\mathrm{d},t,x,y}}{\partial y} = -\beta_{\mathrm{e},x,y} \\ + \frac{\kappa_{\mathrm{s},x,y}}{4\pi}\sum_{l=1}^{N\Omega} w^l I^l_{\mathrm{d},t,x,y}\Phi(\mathbf{\Omega}^m, \mathbf{\Omega}^l) + S_{\mathrm{c},t,x,y}\end{aligned} \tag{10}$$

where ξ and η are directional cosines. w denotes the directional weight. m and l indicate the mth and lth direction. $N\Omega$ represents the number of discretized direction. Thus, the radiative intensity at each grid of computational domain can be obtained by:

$$I^m_{\mathrm{d},t,x,y} = \frac{A^m\partial I^m_{\mathrm{d},t-\Delta t,x,y} + B^m I^m_{\mathrm{d},t,xu,y} + C^m I^m_{\mathrm{d},t,x,yu} + \frac{\kappa_{\mathrm{s},x,y}}{4\pi}w^l I^l_{\mathrm{d},t,x,y}\Phi(\mathbf{\Omega}^m, \mathbf{\Omega}^l) + S_{\mathrm{c},t,x,y}}{A^m + B^m + C^m + \beta_{\mathrm{e},x,y}}, \tag{11}$$

where $A^m = 1/(c\Delta t)$, $B^m = \xi^m/\Delta x$, and $C^m = \eta^m/\Delta y$. The subscript xu and yu represent the upstream positions in the x and y directions. The upstream radiative intensity can be given as:

$$I^m_{\mathrm{d},t,xu,y} = \begin{cases} I^m_{\mathrm{d},t,x-\Delta x,y} & \xi^m > 0 \\ I^m_{\mathrm{d},t,x+\Delta x,y} & \xi^m < 0 \end{cases}, \tag{12}$$

$$I^m_{\mathrm{d},t,x,yu} = \begin{cases} I^m_{\mathrm{d},t,x,y-\Delta y} & \eta^m > 0 \\ I^m_{\mathrm{d},t,x,y+\Delta y} & \eta^m < 0 \end{cases}. \tag{13}$$

To verify the accuracy and reliability of the present solution, a 2D transient radiative transfer problem is considered here. The related parameters of direct problem are listed in Table 1. The reflectance and transmittance signals on the left and right boundaries are compared with those in Ref. [39],

Table 1 Parameters of direct model

Parameters	κ_a	κ_s	ct_p	$c\Delta t$	L_x	L_y	$N_x \times N_y$	$N\Omega$
Units	m^{-1}	m^{-1}	m	m	m	m	–	–
Values	0.002	0.998	0.1	0.002	1.0	1.0	21×21	80

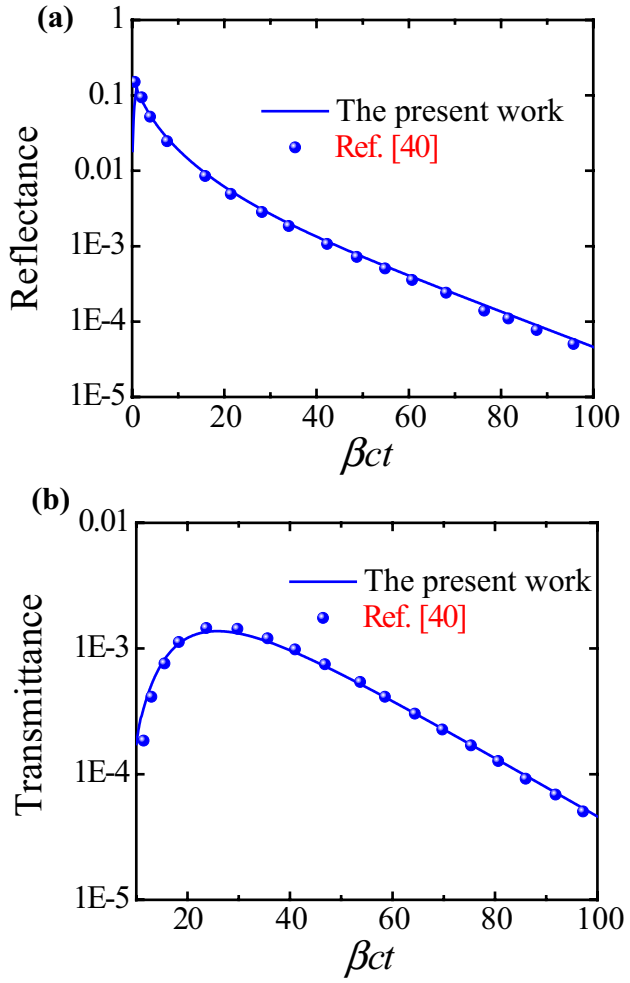

Fig. 2 Verification of the present solution for solving transient radiative transfer problem

which is illustrated in Fig. 2. As shown, good agreements are obtained between the retrieval results and the solutions in reference.

3 Adjoint equation

For the inverse estimation problems, effective and accurate gradient computation is crucial to the whole optimization process. Adjoint equation is an efficient method to get the gradient of objective function with respect to reconstruction parameters, in which the inverse optimization task is transformed into the sensitivity problem and adjoint problem.

3.1 Sensitivity problem

The main goal of this study is to detect the defects in ceramic materials based on optical imaging technique. To reconstruct the absorption and scattering coefficients of media, the exit radiative intensities at boundaries are served as input for the inverse analysis and the objective function is defined as:

$$F_{\text{obj}} = \frac{1}{2}\int_T \mathrm{d}t \int_{\partial D} \mathrm{d}r \left[1 - \frac{R_{\text{est}}(t,\mathbf{r})}{R_{\text{est}}(t,\mathbf{r})}\right]^2 + \mathfrak{R} \tag{14}$$

where T is the total computation time of direct problem. $\mathfrak{R}$ represents the regularization term. R_{est} and R_{exa} represent the estimated and exact emerging radiative intensities at boundaries, which can be expressed as:

$$R(t,\mathbf{r}) = \int_{n\Omega>0} I(t,\mathbf{r})\mathbf{n}\cdot\mathbf{\Omega}\mathrm{d}\Omega. \tag{15}$$

The Gaussian Markov random field is employed as the regularization term which can be written as [40]:

$$\mathfrak{R} = \frac{1}{p\vartheta^p}\sum_{\{u,v\}\in N} b_{u-v}|\kappa_u - \kappa_v|^p, \tag{16}$$

where p and ϑ are image sharpness and scale parameters, respectively. N denotes the set of all neighboring pixel pairs. b_{u-v} represents the weight coefficient. κ indicates the absorption or scattering coefficient.

Adjoint equation is derived by considering some physical relation constraints must be satisfied in the minimization process of objective function. For the reconstruction of optical parameters, the physical relation can be described by TRTE. Thus, Eq. (8) is introduced into the objective function and the following Lagrangian formalism can be obtained [41]:

$$F = \frac{1}{2}\int_T \mathrm{d}t \int_{\partial D} \mathrm{d}r \left[1 - \frac{R_{\mathrm{est}}(t,\mathbf{r})}{R_{\mathrm{exa}}(t,\mathbf{r})}\right]^2 + \Re \int_T \mathrm{d}t \int_D \mathrm{d}r \int_{4\pi} \mathrm{d}t\lambda \times \left\{ \left[\frac{n}{c}\frac{\partial}{t} + \boldsymbol{\Omega}\cdot\nabla + \beta_{\mathrm{e}}(\mathbf{r})\right] I_{\mathrm{d}}(\mathbf{r},\boldsymbol{\Omega},t) - \frac{\kappa_{\mathrm{s}}(\mathbf{r})}{4\pi}\int_{4\pi} \mathrm{d}\Omega' I_{\mathrm{d}}(\mathbf{r},\boldsymbol{\Omega}',t)\Phi(\boldsymbol{\Omega},\boldsymbol{\Omega}') - S_{\mathrm{c}}(\mathbf{r},\boldsymbol{\Omega},t)\right\} \quad (17)$$

where λ represents the Lagrangian multiplier in the adjoint model.

Considering a small variation in absorption and scattering coefficient distributions over the whole computational domain, a small variation of objective function is obtained:

$$\Delta F = \int_T \mathrm{d}t \int_{\partial D} \mathrm{d}r \frac{R_{\mathrm{est}}(t,\mathbf{r}) - R_{\mathrm{exa}}(t,\mathbf{r})}{\left[R_{\mathrm{exa}}(t,r)\right]^2}\Delta R_{est}(t,\mathbf{r}) + \Delta\Re \int_T \mathrm{d}t \int_D \mathrm{d}r \int_{4\pi} \mathrm{d}\Omega \lambda \times \left\{ \left[\frac{n}{c}\frac{\partial}{\partial t} + \boldsymbol{\Omega}\cdot\nabla + \beta_{\mathrm{e}}(\mathbf{r})\right] I_{\mathrm{d}}(\mathbf{r},\boldsymbol{\Omega},t) - \frac{\kappa_{\mathrm{s}}(\mathbf{r})}{4\pi}\int_{4\pi} \mathrm{d}\Omega' \Delta I_{\mathrm{d}}(\mathbf{r},\boldsymbol{\Omega}',t)\Phi(\boldsymbol{\Omega},\boldsymbol{\Omega}') + \Delta\beta_{\mathrm{e}}(\mathbf{r}) I_{\mathrm{d}}(\mathbf{r},\boldsymbol{\Omega},t) - \frac{\Delta\kappa_{\mathrm{s}}(\mathbf{r})}{4\pi}\int_{4\pi} \mathrm{d}\Omega' I_{\mathrm{d}}(\mathbf{r},\boldsymbol{\Omega}',t)\Phi(\boldsymbol{\Omega},\boldsymbol{\Omega}')\right\} \quad (18)$$

3.2 Adjoint problem and gradient equation

To remove the ΔI_{d} in Eq. (18), a special Lagrangian multiplier is defined which satisfies:

$$0 = \int_T \mathrm{d}t \int_{\partial D} \mathrm{d}r \frac{R_{\mathrm{est}}(t,\mathbf{r}) - R_{\mathrm{exa}}(t,\mathbf{r})}{\left[R_{\mathrm{exa}}(t,\mathbf{r})\right]^2}\Delta R_{\mathrm{est}}(t,\mathbf{r}) + \int_T \mathrm{d}t \int_D \mathrm{d}r \int_{4\pi} \mathrm{d}\Omega \lambda \times \left\{ \left[\frac{n}{c}\frac{\partial}{t} + \boldsymbol{\Omega}\cdot\nabla + \beta_e(\mathbf{r})\right] \Delta I_{\mathrm{d}}(\mathbf{r},\boldsymbol{\Omega},t) - \frac{\kappa_{\mathrm{s}}(\mathbf{r})}{4\pi}\int_{4\pi} \mathrm{d}\Omega' I_{\mathrm{d}}(\mathbf{r},\boldsymbol{\Omega}',t)\Phi(\boldsymbol{\Omega},\boldsymbol{\Omega}')\right\}. \quad (19)$$

Considering the following integral transformations:

$$\int_T \mathrm{d}t \int_D \mathrm{d}r \frac{R_{\mathrm{est}}(t,\mathbf{r}) - R_{\mathrm{exa}}(t,\mathbf{r})}{[R_{\mathrm{exa}}(t,\mathbf{r})]^2}\Delta R_{\mathrm{est}}(t,\mathbf{r}) = + \int_T \mathrm{d}t \int_D \mathrm{d}r \frac{R_{\mathrm{est}}(t,\mathbf{r}) - R_{\mathrm{exa}}(t,\mathbf{r})}{\left[R_{\mathrm{exa}}(t,\mathbf{r})\right]^2}\frac{R_{\mathrm{exa}}(t,\mathbf{r})}{\partial I}$$

$$\Delta I = -\int_T \mathrm{d}t \int_D \mathrm{d}r \int_{n.\Omega>0} \mathrm{d}\Omega \lambda \mathbf{n}\cdot\boldsymbol{\Omega}\Delta I, \quad (20)$$

$$\int_T \mathrm{d}t \int_D \mathrm{d}r \int_{4\pi} \mathrm{d}\Omega \lambda \frac{n}{c}\frac{\partial \Delta I_{\mathrm{d}}}{\partial t} = \frac{n}{c}\left[\int_D \mathrm{d}r \int_{4\pi} \mathrm{d}\Omega \frac{n}{c}(\lambda \Delta I_{\mathrm{d}})|_0^{t\max} - \int_T \mathrm{d}t \int_D \mathrm{d}r \int_{4\pi} \mathrm{d}\Omega \Delta I_{\mathrm{d}}\frac{\partial\lambda}{\partial t}\right], \quad (21)$$

$$\int_T \mathrm{d}t \int_D \mathrm{d}r \int_{4\pi} \mathrm{d}\Omega \lambda \boldsymbol{\Omega}\nabla \Delta I_{\mathrm{d}} = \int_T \mathrm{d}t \int_{\partial D} \mathrm{d}r \int_{4\pi} \mathrm{d}\Omega \lambda \Delta I_{\mathrm{d}} \boldsymbol{\Omega}\cdot\mathbf{n} - \int_T \mathrm{d}t \int_D \mathrm{d}r \int_{4\pi} \mathrm{d}\Omega \Delta I_{\mathrm{d}} \boldsymbol{\Omega}\nabla\lambda, \quad (22)$$

Eq. (19) can be written as:

$$0 = \int_T \mathrm{d}t \int_{\partial D} \mathrm{d}r \int_{4\pi} \mathrm{d}\Omega\, \Delta I_{\mathrm{d}} \left\{ \left[-\frac{n}{c}\frac{\partial}{t} + \boldsymbol{\Omega}\cdot\nabla + \beta_{\mathrm{e}}(\mathbf{r})\right]\lambda - \frac{\kappa_{\mathrm{s}}(\mathbf{r})}{4\pi}\int_{4\pi} \mathrm{d}\Omega'\, \lambda\Phi(\boldsymbol{\Omega},\boldsymbol{\Omega}')\right\}. \quad (23)$$

Hence, the Lagrangian multiplier equation can be expressed as:

$$\left[\frac{n}{c}\frac{\partial\lambda}{t} - \boldsymbol{\Omega}\cdot\nabla + \beta_e(\mathbf{r})\right]\lambda + \frac{\kappa_s(\mathbf{r})}{4\pi}\int_{4\pi} \mathrm{d}\Omega'\,\lambda\Phi(\boldsymbol{\Omega},\boldsymbol{\Omega}') = 0. \tag{24}$$

Reverse time from $t = t_{\max}$ to 0 and radiative transfer direction Ω, Eq. (24) can be transformed to:

$$\frac{n}{c}\frac{\partial\lambda}{\partial t} + \boldsymbol{\Omega}\cdot\nabla\lambda = -\beta_e(\mathbf{r})\lambda + \frac{\kappa_s(\mathbf{r})}{4\pi}\int_{4\pi} \mathrm{d}\Omega'\,\lambda\Phi(\boldsymbol{\Omega},\boldsymbol{\Omega}') = 0, \tag{25}$$

which is similar to the TRTE. Thereby, the DOM is also suitable for solving the above Lagrangian multiplier equation. After the Lagrangian multiplier is obtained, the gradient of objective function with respect to absorption and scattering coefficients can be defined as:

$$\Psi_a\frac{\Delta F}{\Delta\kappa_a} = \int_T \mathrm{d}t\int_D \mathrm{d}r\int_{4\pi} \mathrm{d}\Omega\,\lambda(\mathbf{r},\boldsymbol{\Omega},t)I_d(\mathbf{r},\boldsymbol{\Omega},t) + \mathfrak{R}_\kappa, \tag{26}$$

$$\Psi_s = \frac{\Delta F}{\Delta\kappa_s} = \int_T \mathrm{d}t\int_D \mathrm{d}r\int_{4\pi} \mathrm{d}\Omega\,\lambda(\mathbf{r},\boldsymbol{\Omega},t) \left[I_d(\mathbf{r},\boldsymbol{\Omega},t) - \frac{1}{4\pi}\int_{4\pi} \mathrm{d}\Omega' I_d(\mathbf{r},\boldsymbol{\Omega}',t)\Phi(\boldsymbol{\Omega},\boldsymbol{\Omega}')\right] + \mathfrak{R}_\kappa \tag{27}$$

where $\mathfrak{R}_\kappa$ is the differential coefficient of $\mathfrak{R}$ with respect to reconstruction parameters, which can be written as:

$$\mathfrak{R}_\kappa = \begin{cases} \frac{1}{\vartheta^p}\sum\limits_{\{u,v\}\in N} b_{u-v}\left|\kappa_u - \kappa_v\right|^{p-1} & \kappa_u > \kappa_v \\ 0 & \kappa_u = \kappa_v \\ -\frac{1}{\vartheta^p}\sum\limits_{\{u,v\}\in N} b_{u-v}\left|\kappa_u - \kappa_v\right|^{p-1} & \kappa_u < \kappa_v \end{cases}. \tag{28}$$

The detailed computational procedure of adjoint equation has been introduced in Ref [41]. and not repeated here.

4 Sequential quadratic programming

SQP algorithm is one of the most effective inverse techniques for solving constrained optimization tasks. The optimization problem is transformed to a series of quadratic programming (QP) subproblems, through which the algorithm superlinearly converge to the optimum. Considering the following nonlinear constrained optimization problem:

$$\begin{aligned} &\min\ F(x) \\ &\text{s.t}\ c_i(x) = 0\ i \in E = \{1,2,\ldots,m_e\} \\ &c_i(x) = 0\ i \in I = \{m_e+1, m_e+2,\ldots,m\}, \end{aligned} \tag{29}$$

where c_i are restrictions. m and m_e represent the numbers of total restriction and equality restriction, respectively. The optimization is transformed to the following QP subproblem [42]:

$$\begin{aligned} &\min\ \nabla F(x^k)^T d + \tfrac{1}{2}\,d^T H^k d \\ &\text{s.t}\ c_i(x^k) + \nabla c_i\,(x^k)^T d = 0\ \ i \in E \\ &\quad c_i(x^k) + \nabla c_i(x^k)^T d \geqslant 0\ i \in I, \end{aligned} \tag{30}$$

where d represents the search direction at kth iteration. x^k represents the reconstruction parameters at the current iteration. H^k is the approximation of the Hessian of the following Lagrangian:

$$L(x,u) = F(x) - \sum_{i=1}^{m} u_i c_i(x), \tag{31}$$

where u_i is the Lagrangian multiplier in SQP. To ensure H^k is the effective approximation, the following update is used [43]:

$$H^{k+1} = H^k + \frac{\tilde{y}(\tilde{y}^k)^T}{(\tilde{y}^k)^T s^k} - \frac{H^k s^k (s^k)^T H^k}{(s^k) H^k s^k}, \tag{32}$$

where $\tilde{y}^k = \theta y^k + (1-\theta)H^k s^k$, $s^k = s^{k+1} - x^k$, θ and y^k are defined as:

$$\theta = \begin{cases} 1 & (s^k)^T y^k \geqslant \beta(s^k)^T H^k s^k \\ (1-\beta)(s^k)^T H^k s^k \Big/ \left[(s^k)^T H^k s^k - (s^k)^T y^k\right] & (s^k)^T y^k < \beta(s^k)^T H^k s^k \end{cases}, \tag{33}$$

$$y^k = \nabla_x L(x^{k+1}, u^{k+1}) - \nabla_x L(x^k, u^{k+1}), \tag{34}$$

where β is a positive constant $0.1 \leqslant \beta \leqslant 0.2$.

To improve the global convergence of SQP algorithm, the following penalty function is considered [44]:

$$F_p(x) = F(x) + r\left[\sum_{i=1}^{m_e}\left|c_i(x)\right| + \sum_{i=m_e+1}^{m}\left|\min\{0, c_i(x)\}\right|\right], \tag{35}$$

where r is the penalty factor, $r > 0$. Thus, the newly generated reconstruction parameter can be expressed as:

$$x^{k+1} = x^k + \alpha^k d^k, \tag{36}$$

where α^k is search step size, which satisfies:

$$F_p(x^k + \alpha^k d^k) < F_p(x^k) + \beta\alpha^k \left[\overline{F_p}(x^k, d^k) - F_p(x^k)\right] \tag{37}$$

where

$$\overline{F_p}(x^k, d^k) = F(x^k) + \nabla F(x^k)^T + \frac{1}{2} d^T H^k d + r\left[\sum_{i=1}^{m_e} \left|c_i(x^k) + \nabla c_i(x^k)^T d\right| + \sum_{i=m_e+1}^{m} \left|\min\{0, c_i(x)\} + \nabla c_i(x^k)^T d\right|\right]. \tag{38}$$

Moreover, to make sure the global and superlinear convergence of SQP algorithm, the following QP subproblem is employed to replace Eq. (29) when Maratos effect appears [45]:

$$\begin{aligned} &\min\ \nabla(p^k)^T d + \tfrac{1}{2} d^T H^k d \\ &\text{s.t}\ c_i(x^k) + (a_i^k)^T d = 0\ \ i \in E \\ &\quad c_i(x^k) + (a_i^k)^T d \geqslant 0\ i \in I, \end{aligned} \tag{39}$$

where p^k and a^k are defined as:

$$p^k = \nabla F(x^k) + \frac{1}{2} \sum_{i=1}^{m} u^{k+1} \left[\nabla c_i(x^k + \hat{d}^k) - \nabla c_i(x^k)\right] \tag{40}$$

$$a_i^k = \nabla c_i(x^k) + \frac{1}{2} \hat{d}^k \left[\nabla c_i(x^k + \hat{d}^k) - \nabla c_i(x^k)\right] \tag{41}$$

where $\hat{d}^k$ is the solution of Eq. (39). Therefore, the reconstruction parameter and search step size can be generated by:

$$x^{k+1} = x^k + \alpha^k d^k + (\alpha^k)^2 (\hat{d}^k - d^k), \tag{42}$$

$$F_p(x^{k+1}) < F_p(x^k) + \beta\alpha^k [\overline{F}_p(x^k, d^k) - F_p(x^k)]. \tag{43}$$

The iteration stops until one of the following convergence criteria is satisfied:

$$k = k_{\max}, \tag{44}$$

$$\begin{aligned} &\nabla F(x^{k+1}) - \sum_{i=1}^{m} u_i^{k+1} \nabla c_i(x^{k+1}) \leqslant \varepsilon_1 \\ &\left|c_i(x^{k+1})\right| \leqslant \varepsilon_1 \\ &c_i(x^{k+1}) \geqslant \varepsilon_1, \end{aligned} \tag{45}$$

$$\frac{F_p(x^k) - F(x^{k+1})}{\upsilon + \left|F_p(x^{k+1})\right|} \leqslant \varepsilon_2, \tag{46}$$

where $k_{\max}$ denotes the specified maximum iteration number. ε_1, ε_2 and υ are small positive values.

5 Results and discussion

5.1 Description of non-destructive testing

The main purpose of this study is to show the validity of mid-infrared ultrashort-pulse laser in NDT of ceramics based on transient radiative transfer model. As shown in Fig. 3, a 2D square ceramic material with size of $L_x \times L_y = 0.04 \times 0.04\,\mathrm{m}^2$ is considered. The power density of incident laser is set as 3544 W/m^2, and the pulse width of laser is 0.1 ns. Two kinds of reticulated porous ceramics, PS ZrO_2 and OB SiC, are employed as the test materials. Since the difference between the absorption and scattering coefficients is relatively small at the end of the spectral range studied in Ref. [1], the single-wavelength pulse lasers at wavelengths 5.0 and 4.9 μm are selected as the incident source for the NDT of PS ZrO_2 and OB SiC, respectively. Hendricks and Howell [1] experimentally

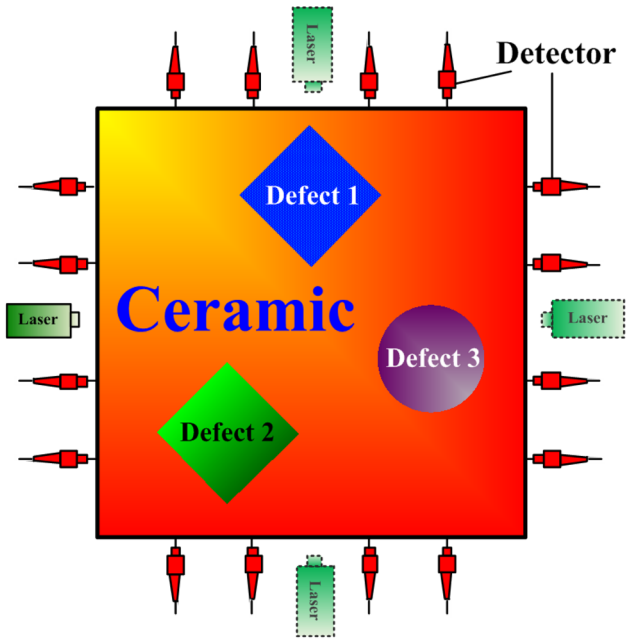

Fig. 3 Schematic of non-destructive testing

Table 2 Optical parameters of ceramics and air

Material	Wavelength (μm)	Phase function	f_{is}	f_{bck} or g_{hg}	κ_a (m^{-1})	κ_s (m^{-1})
PS ZrO_2	5.0	DRIFD	0.67	0.02	71.3	461.1
		H–G	0.01	0.48	85.7	680.1
OB SiC	4.9	DRIFD	0.11	0.00	100.5	531.3
		H–G	0.00	0.75	193.0	325.6
Air	–	Isotropic	1.0	0.0	0.0	0.0

investigated the absorption and scattering coefficients of PS ZrO_2 and OB SiC for DRIFD and modified H–G phase functions and the related optical properties are listed in Table 2.

The emerging radiative intensities from four boundaries are employed as the measurement signals to reconstruct the absorption and scattering coefficient distributions. Since measurement errors are inevitable, the random standard deviation is considered which can be expressed as:

$$Y_{mea} = Y_{exa} + \sigma\varsigma, \tag{47}$$

where Y_{mea} and Y_{exa} are the measurement signals with and without random error, respectively. ς represents a random variable of normal distribution with zero mean and unit standard deviation. The standard deviations of measured radiative signals, σ for a γ % measured error at 99% confidence, are determined as:

$$\sigma = \frac{Y_{exa} \times \gamma\%}{2.576}, \tag{48}$$

where the denominator is set as 2.576, because a normally distributed population is contained within ±2.576 standard deviation of the mean.

To evaluate the overall accuracy of the reconstruction results, the normalized root-mean square error (NRMSE) is introduced which is defined as [46]:

$$\mathrm{NRMSE} = \sqrt{\sum_{i=1}^{NN}(x_i - \widetilde{x}_i)^2} \Big/ \sqrt{\sum_{i=1}^{N} x_i^2}, \tag{49}$$

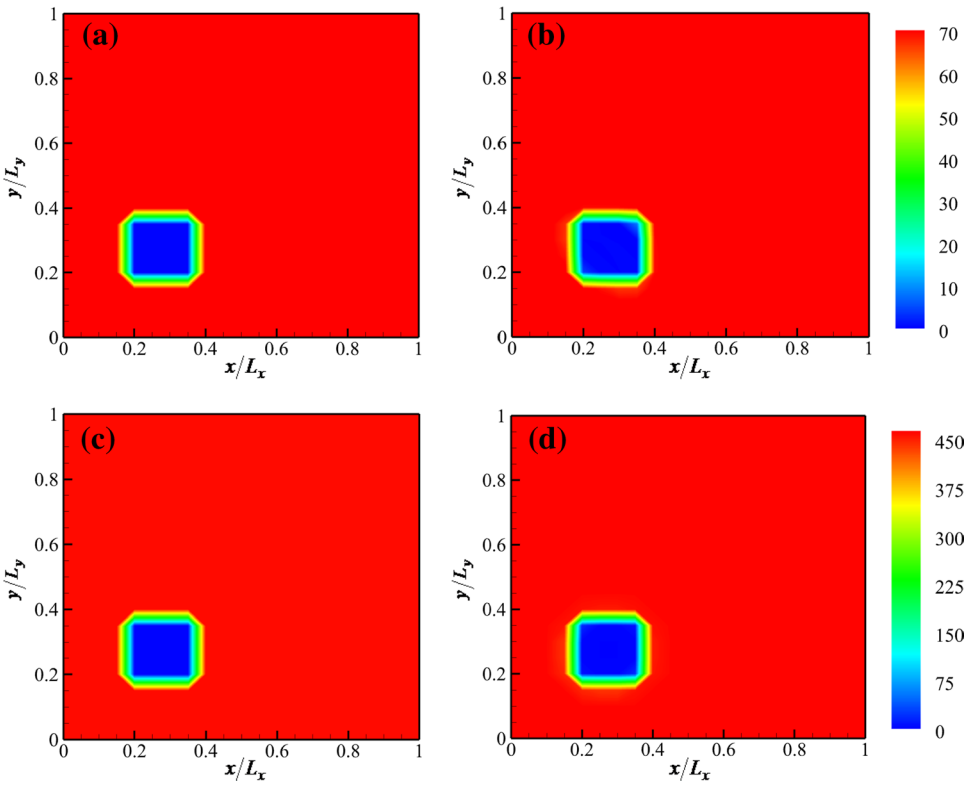

Fig. 4 Reconstruction results of Test 1 for DRIFD phase function. **a** Real distribution of absorption coefficient; **b** retrieved results of absorption coefficient; **c** real distribution of scattering coefficient; and **d** retrieved results of scattering coefficient

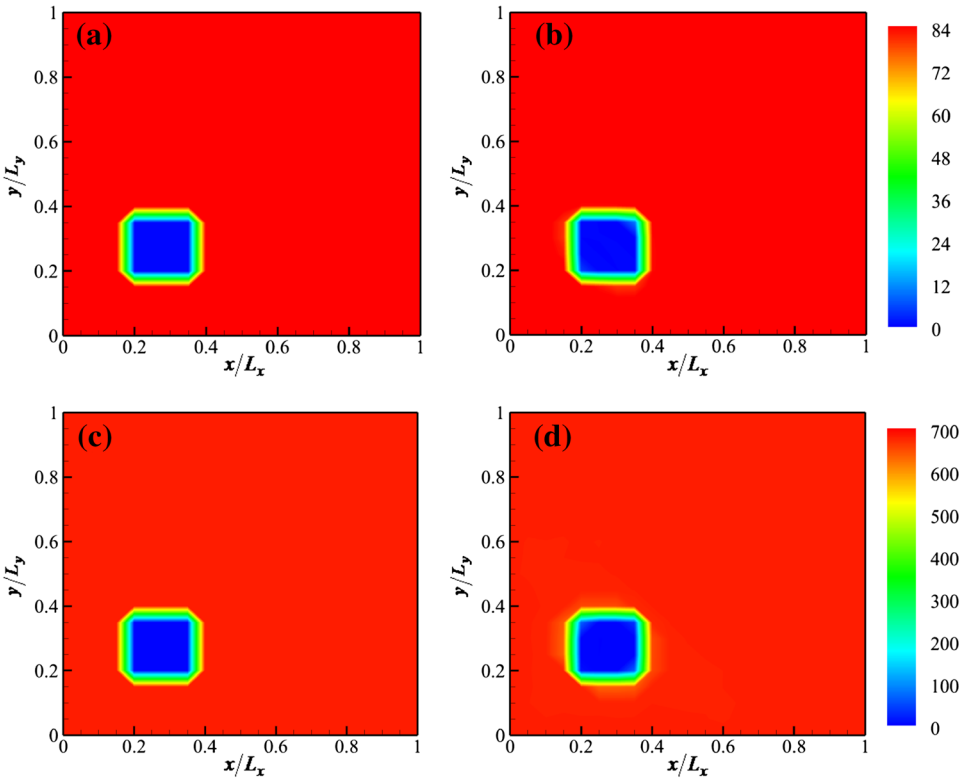

Fig. 5 Reconstruction results of test 1 for H–G phase function. **a** Real distribution of absorption coefficient; **b** retrieved results of absorption coefficient; **c** real distribution of scattering coefficient; and **d** retrieved results of scattering coefficient

where x_i and $\widetilde{x}_i$ represent the exact and estimated values of the reconstruction parameters. *NN* is the total number of the estimation parameters.

All cases are implemented using the Fortran code, and the developed program is executed on an Intel Core(TM) i7-7700 PC.

5.2 Non-destructive testing of PS ZrO_2

To verify the feasibility of the present inverse technique in NDT of ceramics, a square air defect is considered firstly. In Test 1, the defect is located at the bottom left of media whose central coordinate is set as $x_c/L_x = 0.25$ and $y_c/L_y = 0.25$. The reconstruction results of PS ZrO_2 for DRIFD and H–G phase functions are illustrated in Figs. 4 and 5, respectively. As shown, all the characteristics including optical properties, geometric shape and spatial position of the defect can be accurately reconstructed. From the reconstruction results, the air defect in ceramic can be accurately identified, which demonstrates the validity of inverse transient radiative transfer technique in NDT of ceramic materials.

The effect of the central position of defect is also investigated and the settings of central coordinates are shown in Table 3. All the defects at different positions can be accurately reconstructed (see Figs. 6, 7, 8, 9), from which the defects in ceramics can be clearly determined. The NRMSEs of reconstruction results for different central positions and different phase functions are pretty close and the maximum NRMSE is less than 0.012 (see Table 4), which demonstrates that the present solution can be successfully applied to the NDT of ceramics. Since the retrieval results for DRIFD and H–G phase functions are analogous, the following discussions of this study are based on H–G phase function.

Moreover, the NDT results of ceramic with multi-defects (three defects) are studied (see Fig. 10). Although the imaging quality slightly decreases, the retrieved results can accurately reflect the defects in ceramic materials. Therefore, the NDT technique based on transient radiative transfer model is also effective in detecting multiple defects in ceramic materials. Table 5 lists the NRMSE values and computational time for different sampling times of direct problem. As shown, the longer the sampling time is, the smaller the

Table 3 Central coordinates of defect in ceramic

	x_c/L_x	y_c/L_y
Test 2	0.475	0.725
Test 3	0.725	0.475

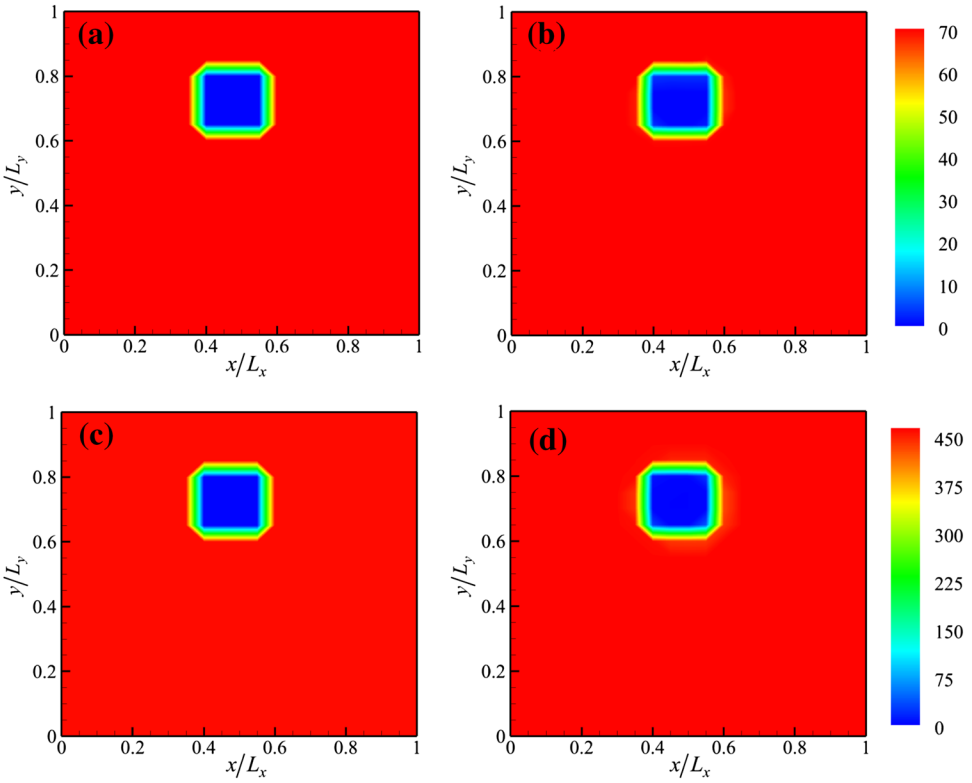

Fig. 6 Reconstruction results of test 2 for DRIFD phase function. **a** Real distribution of absorption coefficient; **b** retrieved results of absorption coefficient; **c** real distribution of scattering coefficient; and **d** retrieved results of scattering coefficient

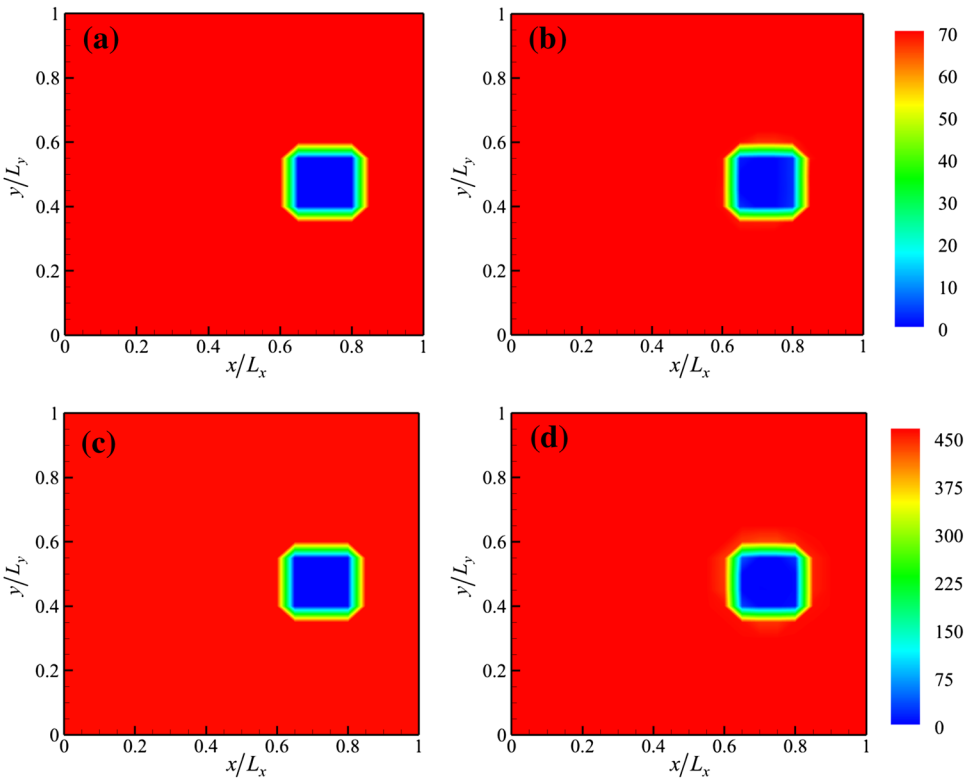

Fig. 7 Reconstruction results of test 3 for DRIFD phase function. **a** Real distribution of absorption coefficient; **b** retrieved results of absorption coefficient; **c** real distribution of scattering coefficient; and **d** retrieved results of scattering coefficient

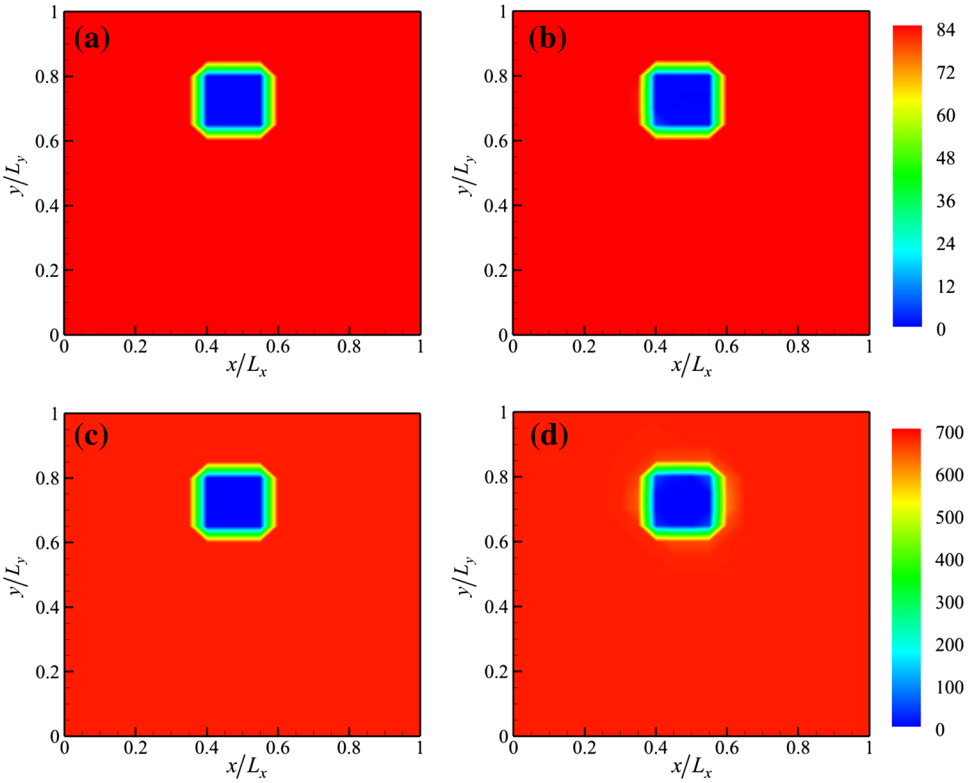

Fig. 8 Reconstruction results of test 2 for H–G phase function. **a** Real distribution of absorption coefficient; **b** retrieved results of absorption coefficient; **c** real distribution of scattering coefficient; and **d** retrieved results of scattering coefficient

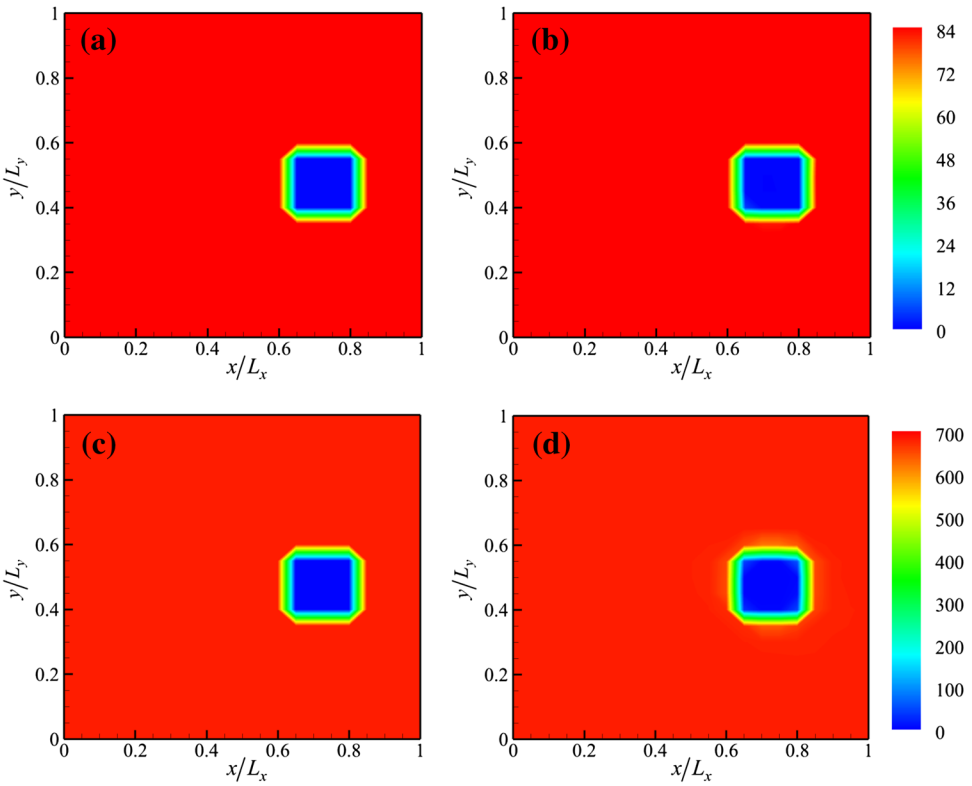

Fig. 9 Reconstruction results of test 3 for H–G phase function. **a** Real distribution of absorption coefficient; **b** retrieved results of absorption coefficient; **c** real distribution of scattering coefficient; and **d** retrieved results of scattering coefficient

Table 4 The NRMSE of reconstruction results for PS ZrO_2

Phase function	Test	NRMSE	
		κ_a	κ_s
DRIFD	Test 1	0.0089	0.0063
	Test 2	0.0081	0.0096
	Test 3	0.0083	0.0095
H–G	Test 1	0.0093	0.0115
	Test 2	0.0049	0.0119
	Test 3	0.0046	0.0117

Table 5 The NRMSE values and computational time for different sampling times

Sampling time (ns)	Computational time (s)	NRMSE	
		κ_a	κ_s
40	558.26	0.0436	0.0212
60	651.34	0.0386	0.0275
80	770.06	0.0263	0.0382
100	833.65	0.0233	0.0355
150	1077.50	0.0232	0.0354

NRMSE will be, whereas the longer the total computational time will be. Considering the imaging accuracy and computational time synthetically, the sampling time is set as 100 ns.

5.3 Non-destructive testing of OB SiC

Since the principle of NDT technique for OB SiC is similar to that for PS ZrO_2, only two and three defects are considered in this section. As shown in Figs. 11 and 12, all the defects in OB SiC can be accurately identified by the present model. The edges and positions of defects can be clearly determined based on the imaging results, which means the NDT technique in this study is effective and robust to detect the defects in ceramic materials.

To test the robustness of the inverse technique, random errors are added into the measurement signals. Figures 13 and 14 show the reconstruction results of absorption and scattering coefficients for different measurement errors. Although the random error is increased to 50%, the positions and optical properties of defects can also be distinguished according to the imaging results. It is worth noting that the excessive imaging errors on the boundaries in Fig. 14c, d are caused by the incident laser. Table 6 lists the NRMSE values of retrieval results for different measurement errors. The NRMSE increases with the increase

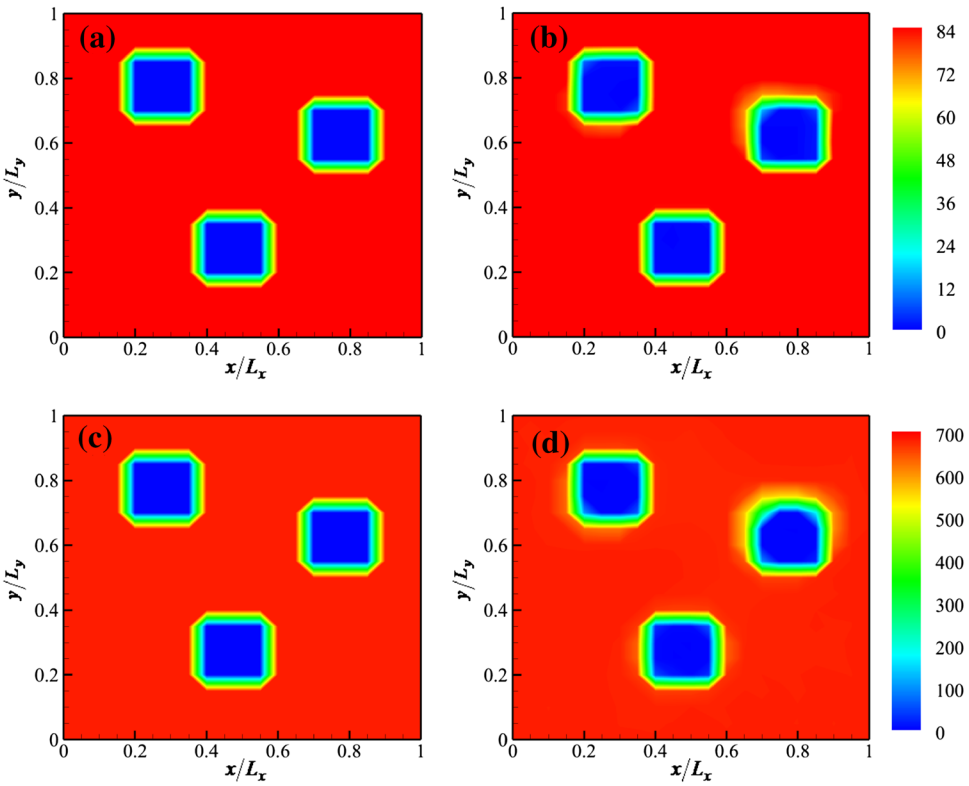

Fig. 10 Reconstruction result of PS ZrO2 with three defects. **a** Real distribution of absorption coefficient; **b** retrieved results of absorption coefficient; **c** real distribution of scattering coefficient; and **d** retrieved results of scattering coefficient

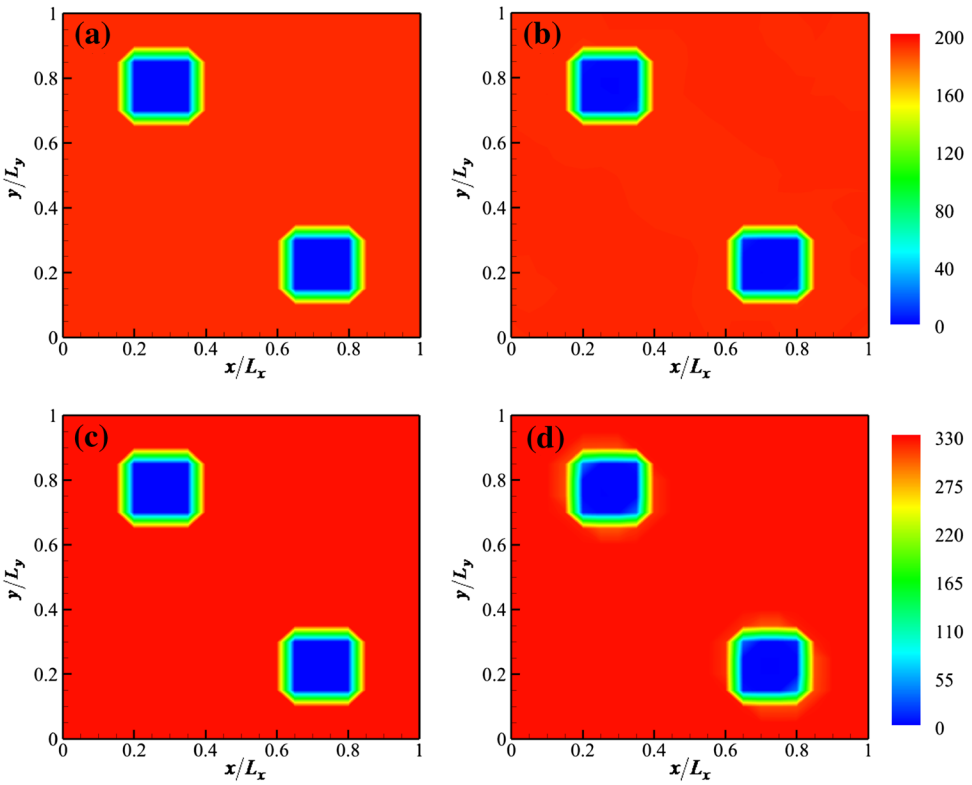

Fig. 11 Reconstruction result of OB SiC with two defects. **a** Real distribution of absorption coefficient; **b** retrieved results of absorption coefficient; **c** real distribution of scattering coefficient; and **d** retrieved results of scattering coefficient

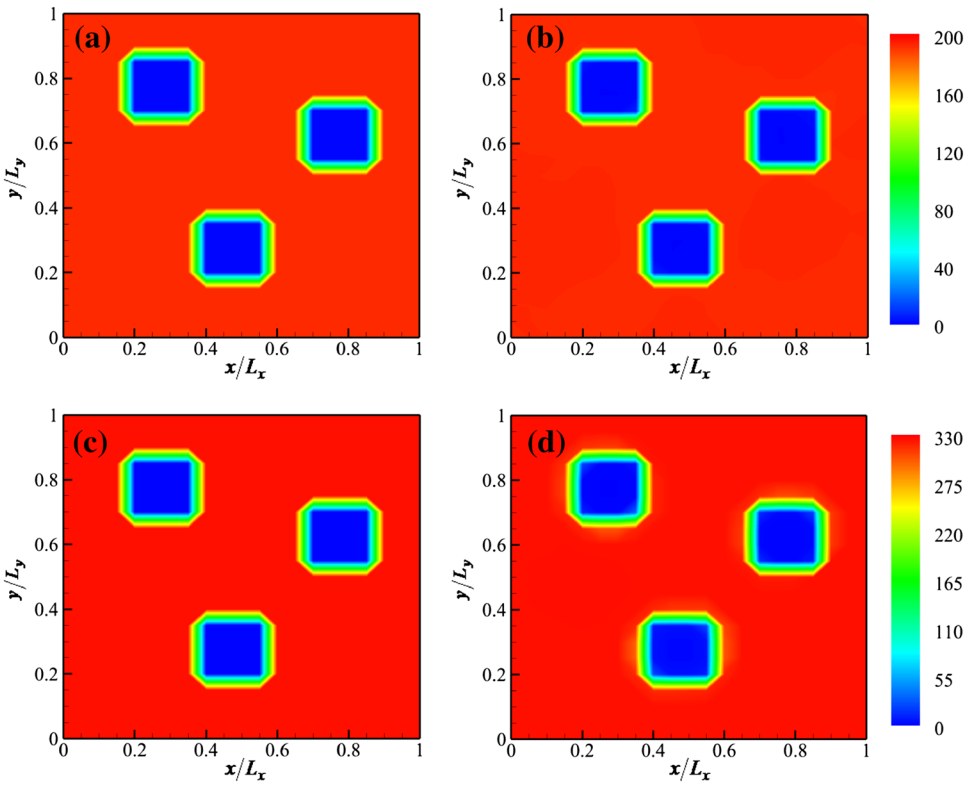

Fig. 12 Reconstruction result of OB SiC with three defects. **a** Real distribution of absorption coefficient; **b** retrieved results of absorption coefficient; **c** real distribution of scattering coefficient; and **d** retrieved results of scattering coefficient

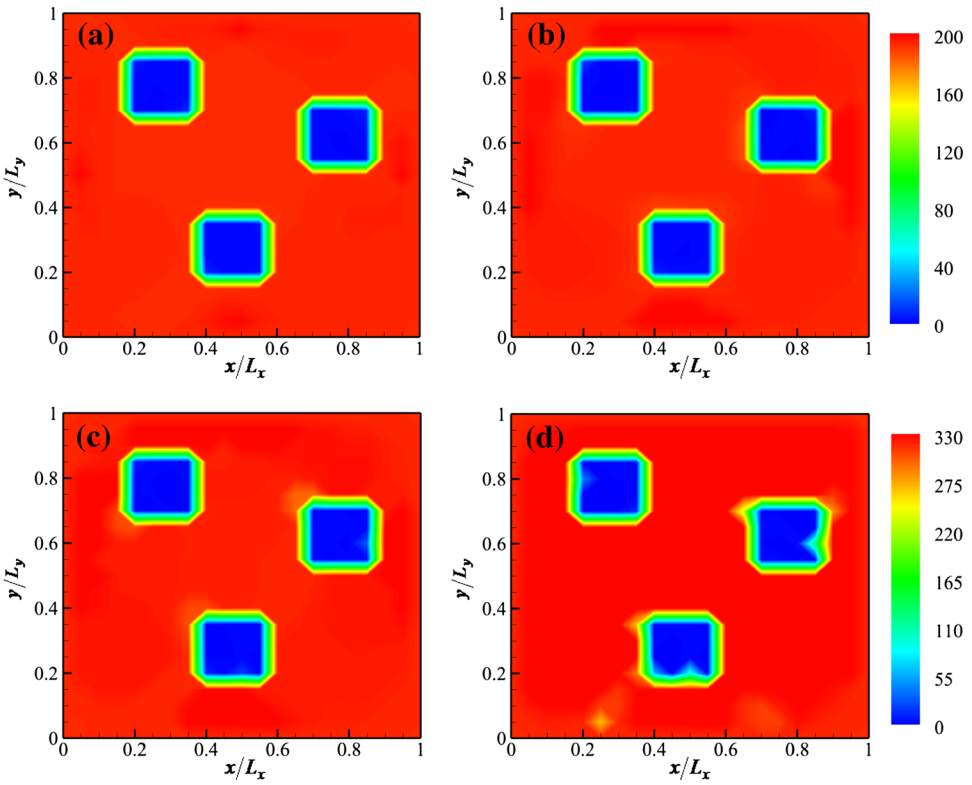

Fig. 13 Reconstruction results of absorption coefficient of OB SiC for **a** 5%, **b** 10%, **c** 20%, and **d** 50% measurement errors

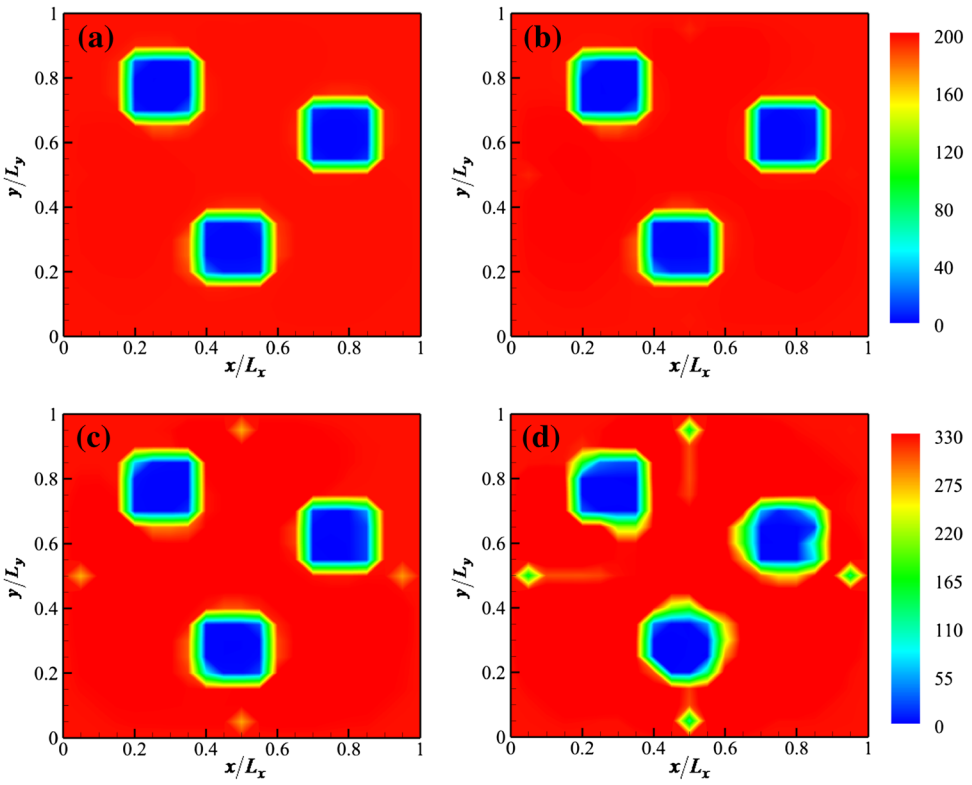

Fig. 14 Reconstruction results of scattering coefficient of OB SiC for **a** 5%, **b** 10%, **c** 20%, and **d** 50% measurement errors

Table 6 The NRMSE values of reconstruction results for different measurement errors

Measurement error (%)	NRMSE	
	κ_a	κ_s
0	0.0027	0.0123
5	0.0065	0.0144
10	0.0138	0.0156
20	0.0199	0.0328
50	0.0449	0.1146

of random error. The maximum NRMSE is only 0.1146, which demonstrates that the present technique has strong robustness.

Furthermore, the NDT of OB SiC for circular and oval defects is investigated (see Fig. 15). Both the circular and oval defects are accurately reconstructed. The retrieved absorption and scattering coefficient distributions by the inverse technique are in good agreement with the real distributions. Comparing Fig. 15b, c, e, f with a, d, it can be found that the differences of edges are caused by the coarse grids. Thus, locally refining meshes around defects to get smooth edges is our further research interest.

6 Conclusions

The mid-infrared ultrashort-pulse laser is employed to nondestructively detect the defects in ceramic materials based on the transient radiative transfer model. The direct problem is solved by DOM and the obtained exit radiative intensity on boundary is served as measurement signals. The adjoint equation model is applied to get the gradient of objective function with respect to absorption and scattering coefficients and the SQP algorithm is used to optimize the objective function. Two reticulated porous ceramics including PS ZrO_2 and OB SiC are selected as the testing materials. The retrieved results show that the boundaries, positions and radiative properties of defects can be accurately identified. The effects of spatial position, total number and geometric shape of defects on the imaging results are investigated. All the reconstructed absorption and scattering coefficients are in good agreement with the real distributions. Even though the measurement error is increased to 50%, the NRMSE is only 0.1146 and the defects can be accurately determined by the reconstruction results, which demonstrates the present technique is effective and robust in NDT of ceramics.

The further research direction is to investigate the locally refining meshes technique to get the smooth edges of defects.

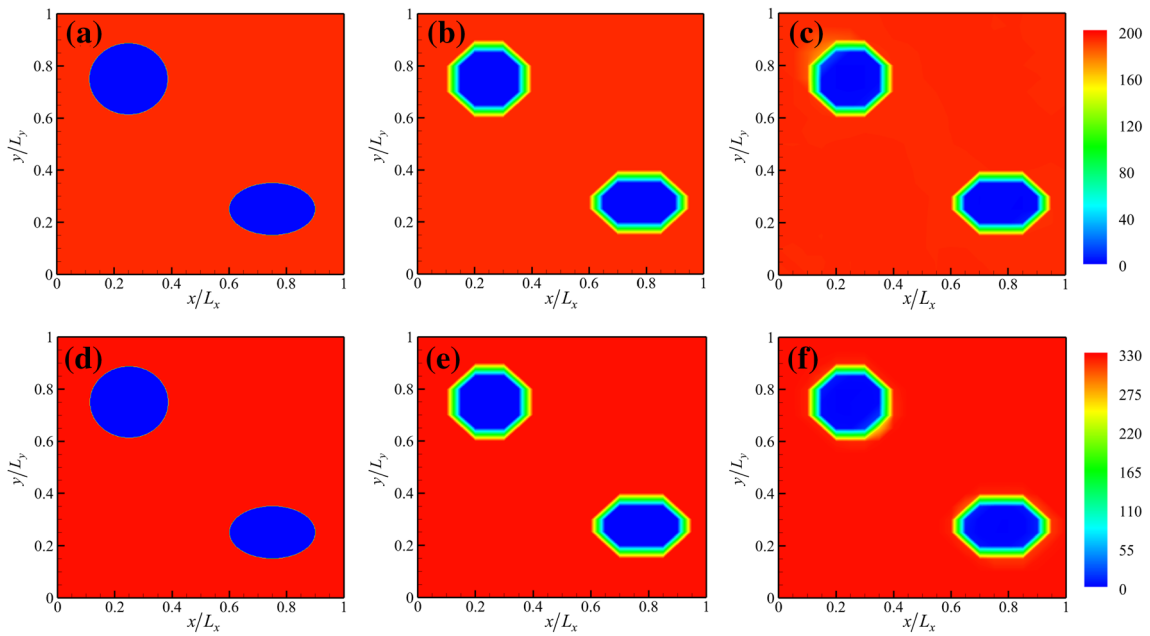

Fig. 15 Reconstruction results of circular and oval defects in OB SiC. **a** Real distribution of absorption coefficient for 501 × 501 grids; **b** real distribution of absorption coefficient for 21 × 21 grids; **c** retrieved distribution of absorption coefficient for 21 × 21 grids; **d**rReal distribution of scattering coefficient for 501 × 501 grids; **e** real distribution of scattering coefficient for 21 × 21 grids; and **f** retrieved distribution of scattering coefficient for 21 × 21 grids

Acknowledgements The supports of this work by the National Natural Science Foundation of China (No. 51576053) is gratefully acknowledged. A very special acknowledgement also to the editors and referees who made important comments to improve this paper.

References

1. T.J. Hendricks, J.R. Howell, Absorption/scattering coefficients and scattering phase functions in reticulated porous ceramics. ASME J. Heat Transf. **118**(1), 79–87 (1996)
2. J. Rebelo Kornmeier, M. Hofmann, S. Schmidt, Non-destructive testing of satellite nozzles made of carbon fibre ceramic matrix composite, C/SiC. Mater. Charact. **58**(10), 922–927 (2007)
3. S. Petit, M. Duquennoy, M. Ouaftouh, F. Deneuville, M. Ourak, S. Desvaux, Non-destructive testing of ceramic balls using high frequency ultrasonic resonance spectroscopy. Ultrasonics **43**(10), 802–810 (2005)
4. B. Zhang, C.L. Xu, S.M. Wang, An inverse method for flue gas shielded metal surface temperature measurement based on infrared radiation. Meas. Sci. Technol. **27**(7), 074002 (2016)
5. J.L. Gong, J.Y. Liu, L. Qin, Y. Wang, Investigation of carbon fiber reinforced polymer (CFRP) sheet with subsurface defects inspection using thermal-wave radar imaging (TWRI) based on the multi-transform technique. NDT&E Int. 62, 130–136 (2014)
6. D.J.W. Klunder, E. Krioukov, F.S. Tan, T. van der Veen, H.F. Bulthuis, G. Sengo, C. Otto, H.J.W.M. Hoekstra, A. Driessen, Vertically and laterally waveguide-coupled cylindrical microresonators in Si3N4 on SiO2 technology. Appl. Phys. B **73**(5–6), 603–608 (2014)
7. G.L. Yuan, S.W. Or, J.M. Liu, Z.G. Liu, Structural transformation and ferroelectromagnetic behavior in single-phase $Bi_{1-x}Nd_xFeO_3$ multiferroic ceramics. Appl. Phys. Lett. **89**(5), 052905 (2006)
8. Y.K. Zhu, G.Y. Tian, R.S. Lu, H. Zhang, A review of optical NDT technologies. Sensors **11**(8), 7773–7798 (2011)
9. J.Y. Liu, L. Qin, Q.J. Tang, Y. Wang, Experimental study of inspection on a metal plate with defect using ultrasound lock-in thermographic technique. Infrared Phys. Technol. **55**(4), 284–291 (2012)
10. R. Dsouza, H.M. Subhash, K. Neuhaus, J. Hogan, C. Wilson, M. Leahy, 3D nondestructive testing system with an affordable multiple reference optical-delay-based optical coherence tomography. Appl. Opt. **54**(18), 5634–5638 (2015)
11. T.H. Wei, D.J. Hagan, M.J. Sence, E.W. Van Stryland, J.W. Perry, D.R. Coulter, Direct measurements of nonlinear absorption and refraction in solutions of phthalocyanines. Appl. Phys. B **54**(1), 46–51 (1992)
12. R.E. Alvarez, A. Macovski, Energy-selective reconstructions in X-ray computerised tomography. Phys. Med. Biol. **21**(5), 733–744 (1976)
13. L.-S. Chang, T.-H. Chuang, Ultrasonic testing of artificial defects in alumina ceramic. Ceram. Int. **23**(4), 367–373 (1997)
14. M. Ohtsu, M. Shigeishi, H. Iwase, W. Koyanagit, No access determination of crack location, type and orientation in a concrete structures by acoustic emission. Mag. Concrete Res. **43**(155), 127–134 (1991)
15. K.F. Schmidt, R.M. Goitia, W.A. Ellingson, W. Green, Correlation of scanning microwave interferometry and digital X-ray images for damage detection in ceramic composite armor. AIP Conf. Proc. **1430**(1), 1129–1136 (2012)
16. S. Sfarra, D. Ambrosini, A. Paoletti, D. Paoletti, C. Ibarra-Castanedo, A. Bendada, X. Maldague, Quantitative infrared thermography (IRT) and holographic interferometry (HI): nondestructive testing (NDT) for defects detection in the silicate ceramics industry. Adv. Sci. Technol. Res. J. **68**, 102–107 (2010)
17. S. Pangraz, H. Simon, R. Herzer, W. Arnold, *Non-destructive Evaluation of Engineering Ceramics by High-Frequency Acoustic Techniques*. (Springer, Boston, 1991)
18. J.Y. Liu, J.L. Gong, L. Qin, H.M. Wang, Y. Wang, Study of inspection on metal sheet with subsurface defects using linear frequency modulated ultrasound excitation thermal-wave imaging (LFM-UTWI). Infrared Phys. Technol. **62**, 136–142 (2014)
19. D. Balageas, X. Maldague, D. Burleigh, V.P. Vavilov, B. Oswald-Tranta, J.M. Roche, C. Pradere, G.M. Carlomagno, Thermal (IR) and other NDT techniques for improved material inspection. J. Nondestr. Eval. **35**(1), 18 (2016)
20. J.M. Milne, P. Carter, A transient thermal method of measuring the depths of sub-surface flaws in metals. Br. J. Non-Destr. Test. **30**(5), 333–336 (1988)
21. J.G. Sun, S. Erdman, L. Connolly, Measurement of delamination size and depth in ceramic matrix composites using pulsed thermal imaging, in *27th International cocoa beach conference on advanced ceramics and composites: B: ceramic engineering and science proceedings*, vol. 24, no. 4 (Wiley, Hoboken, 2003), pp. 201–206
22. J.Y. Liu, Q.J. Tang, X. Liu, Y. Wang, Research on the quantitative analysis of subsurface defects for non-destructive testing by lock-in thermography. NDT&E Int. **45**(1), 104–110 (2012)
23. J.Y. Liu, Q.J. Tang, Y. Wang, The study of inspection on SiC coated carbon–carbon composite with subsurface defects by lock-in thermography. Compos. Sci. Technol. **72**(11), 1240–1250 (2012)
24. G. Busse, D. Wu, W. Karpen, Thermal wave imaging with phase sensitive modulated thermography. J. Appl. Phys. **71**(8), 3962–3965 (1992)
25. N. Ludwig, P. Teruzzi, Heat losses and 3D diffusion phenomena for defect sizing procedures in video pulse thermography. Infrared Phys. Technol. **43**(3), 297–301 (2002)
26. X. Maldague, A. Ziadi, M. Klein, Double pulse infrared thermography. NDT&E Int. **37**(7), 559–564 (2004)
27. M. Akamatsu, Z.X. Guo, Ultrafast radiative transfer characteristics in multilayer inhomogeneous 3d media subjected to a collimated short square pulse train. Heat Transf. Res. **47**(7), 633–651 (2016)
28. F.Q. Wang, L.X. Ma, J.Y. Tan, Z.N. Guan, L.H. Liu, Optical constant measurements of solar thermochemical reaction catalysts and optical window. Optik. **131**, 323–334 (2017)
29. S.M.H. Sarvari, A new approach to solve the radiative transfer equation in plane-parallel semitransparent media with variable refractive index based on the discrete transfer method. Int. Commun. Heat Mass Transf. **78**, 54–59 (2016)
30. J.C. Hebden, A. Gibson, T. Austin, R.M. Yusof, N. Everdell, D.T. Delpy, S.R. Arridge, J.H. Meek, J.S. Wyatt, Imaging changes in blood volume and oxygenation in the newborn infant brain using three-dimensional optical tomography. Phys. Med. Biol. **49**(7), 1117–1130 (2004)
31. J. Jiao, Z.X. Guo, Thermal interaction of short-pulsed laser focused beams with skin tissues. Phys. Med. Biol. **54**(13), 4225–4241 (2009)
32. K.Y. Li, S.L. Liu, Functional imaging of breast tissue and clinical application. Wuhan Univ. J. Nat. Sci. **11**(2), 373–376 (2006)
33. S.K. Wan, Z.X. Guo, Correlative studies in optical reflectance measurements of cerebral blood oxygenation. J. Quant. Spectrosc. Radiat. Transf. **98**(2), 189–201 (2006)
34. A. Vogel, J. Noack, G. Hüttman, G. Paltauf, Mechanisms of femtosecond laser nanosurgery of cells and tissues. Appl. Phys. B **81**(8), 1015–1047 (2005)
35. M.F. Modest, *Radiative Heat Transfer*. (McGraw-Hill, New York, 2003)
36. B. Hunter, Z.X. Guo, Improved treatment of anisotropic scattering for ultrafast radiative transfer analysis. ASME J. Heat Transf. **137**(9), 091004 (2015)

37. R. Siegel, J.R. Howell, *Thermal Radiation Heat Transfer*, 3rd edn. (Hemisphere Publishing Corporation, Washington DC, 1992)
38. S.C. Mishra, P. Chugh, P. Kumar, K. Mitra, Development and comparison of the DTM, the DOM and the FVM formulations for the short-pulse laser transport through a participating medium. Int. J. Heat Mass Trasf. **49**(11–12), 1820–1832 (2006)
39. M. Sakami, K. Mitra, P.F. Hsu, Analysis of light pulse transport through two-dimensional scattering and absorbing media. J. Quant. Spectrosc. Radiat. Transf. **73**(2), 169–179 (2002)
40. S.S. Saquib, K.M. Hanson, G.S. Cunningham, Model-based image reconstruction from time-resolved diffusion data, in *Proceedings of SPIE*, (1997), pp. 369–380
41. J. Boulanger, A. Charette, Numerical developments for short-pulsed near infra-red laser spectroscopy. Part II: inverse treatment. J. Quant. Spectrosc. Radiat. Transf. **91**(3), 297–318 (2005)
42. S.P. Han, A globally convergent method for nonlinear programming. J. Optim. Theory Appl. **22**(3), 297–309 (1977)
43. M.J.D. Powell, *The Convergence of Variable Metric methods for Non-linearly Constrained Optimization Calculations*. (Elsevier Inc, Academic Press Inc, University of Wisconsin, Madison, 1978), pp. 27–63
44. K. Schittkowski, The nonlinear programming method of Wilson, Han, and Powell with an augmented Lagrangian type line search function. Numer. Math. **38**(1), 83–114 (1981)
45. M. Fukushima, A successive quadratic programming algorithm with global and superlinear convergence properties. Math. Program. **35**(3), 253–264 (1986)
46. J.C. Ye, K.J. Webb, C.A. Bouman, R.P. Millane, Optical diffusion tomography by iterative-coordinate-descent optimization in a Bayesian framework. J. Opt. Soc. Am. A **16**(10), 2400–2412 (1999)